REPORT
doi:10.26443/seismica.v4i1.1483

SEISMICA

WMSAN Python Package: From Oceanic Forcing to Synthetic Cross-correlations of Microseismic Noise

Lisa Tomasetto * [1], **Pierre Boué** [1], **Fabrice Ardhuin** [2], **Éléonore Stutzmann** [3], **Zongbo Xu** [3], **Raphaël De Plaen** [4], **Laurent Stehly** [1]

[1] Institut des Sciences de la Terre, CNRS, IRD, Université Gustave Eiffel, Université Grenoble Alpes, University of Savoie Mont Blanc, Grenoble, France, [2] Laboratoire d'Océanographie Physique et Spatiale (LOPS), Univ. Brest, CNRS, IRD, Ifremer, IUEM, Brest, France, [3] Université Paris Cité, Institut de physique du globe de Paris, CNRS, Paris, France, [4] Seismology–Gravimetry, Royal Observatory of Belgium, Brussels, Belgium

Abstract Seismic ambient noise spectra ubiquitously show two amplitude peaks corresponding to distinct oceanic wave interaction mechanisms called primary (seismic period (T) ≈ 14s) and secondary (T $\approx$ 7s) microseism. Seismic noise records are used in a wide range of applications including crustal monitoring, imaging of the Earth's deep interior using noise correlations, and studies on the coupling between oceans and solid Earth. All of these applications could benefit from a robust knowledge of spatiotemporal dynamics of microseismic sources. Consequently, seismologists have been studying how to model microseismic sources of ambient noise with the recent improvements in ocean wave models. Global sea state and its derivative products are now covering the past decades in models such as the WAVEWATCHIII hindcast. This paper introduces the Wave Model Sources of Ambient Noise (WMSAN, pronounced *[wam-san]*) Python package. This modular package uses standardized wave model outputs to visualize ambient noise source maps and efficiently compute synthetics of seismic spectrograms and cross-correlations for surface waves (Rayleigh) and body waves (P, SV), in a user-friendly way.

Production Editor:
Yen Joe Tan
Handling Editor:
Paula Koelemeijer
Copy & Layout Editor:
Hannah F. Mark

Received:
September 20, 2024
Accepted:
March 26, 2025
Published:
April 11, 2025

Non-technical summary Continuous shakes of the ground recorded everywhere on Earth, called seismic ambient noise, show significant peaks in energy around 7 s and 14 s of period. These correspond to seismic waves originating from interactions between oceanic waves with themselves or with the sea floor at the coast respectively. Seismic ambient noise studies focus on retrieving information on the structure of the Earth at different scales and depths. Knowing the dynamic of the source of seismic waves is crucial to extracting the physical characteristics of the sampled medium. Recent developments in oceanic wave modeling, through satellite and buoy data integration, have opened new opportunities for seismologists to understand recorded seismic traces. In this study, we introduce the Wave Model Sources of Ambient Noise (WMSAN, pronounced *[wam-san]*) Python package to visualize the maps of ambient noise sources and compute simulated seismic waveforms in an efficient user-friendly fashion.

1 Introduction

Ocean waves and extreme weather conditions have been known to generate oscillations of the Earth recorded continuously on seismographs since early prototypes by Bertelli (1872).

Ocean waves produce energetic signals in three distinct period bands of the noise spectrum, namely the hum with periods larger than 30 s, the primary microseisms that rise around the 14-30 s period band, and the secondary microseisms that are observed in 3-14 s of period (e.g., Hasselmann, 1963; Ardhuin et al., 2015, 2019).

Primary and secondary microseisms have been extensively studied since the mid-twentieth century to explain seismological observations inland, (e.g., Longuet-Higgins, 1950; Hasselmann, 1963). The primary microseism mechanism ensues from the interaction of an oceanic wave train and a topographic bottom close to the coast, which results in seismic waves with a frequency similar to the ocean wave (e.g., Darbyshire and Okeke, 1969; Ardhuin, 2018). The secondary microseism mechanism, which is the most energetic in amplitude, results from a nonlinear interaction between wave trains traveling in opposite directions with similar oscillating periods; the resulting seismic waves present frequencies at twice the oceanic wave frequencies (e.g., Longuet-Higgins, 1950; Hasselmann, 1963; Kibblewhite and Ewans, 1985).

Hum was the least understood phenomenon, perhaps because it was discovered much later than the others. Several hypotheses have been developed involving the generation of primary and secondary microseism or resonance between the atmosphere and solid Earth (e.g., Fukao et al., 2010; Nishida, 2013, 2014). Nevertheless, the hum generation mechanisms seem similar to the primary microseism, caused by interactions of infragravity waves with a sloping bottom at continental shelves. This hypothesis is the most quantitatively valid when comparing modeled and data time series (e.g., Ardhuin et al., 2015, 2019). The WMSAN package focuses on modeling sources of seismic waves in the secondary microseismic band.

Seismic noise has been of great interest among seismologists in the last decades with the development of seismic interferometry, where cross-correlations of seismic signals are used for imaging and monitoring (e.g., Sabra et al., 2005; Bensen et al., 2007; Lin et al., 2008; Haned et al., 2016). Assuming implicitly a favorable distribution of noise sources, noise correlations in the secondary microseism band, but not exclusively in that band, have been used in a wide range of applications such as imaging the Earth at different scales (e.g., Lu et al., 2018; Boué et al., 2013) and monitoring the evolution of the crust (e.g., Brenguier et al., 2008). However, the dynamic of noise sources breaks such assumptions and thus may bias measurements: in particular, some studies have shown that global microseismic sources follow a seasonal pattern that impacts cross-correlations (e.g., Stehly et al., 2006; Igel et al., 2023; Valero Cano et al., 2024).

Secondary microseismic sources are distributed globally, with strong sources in the Northern Hemisphere from October to March and strong sources in the Southern Hemisphere from April to September. Punctual direct observations of both surface and body waves from these sources were reported for extreme cyclones (e.g., Oliver, 1962; Vinnik, 1973). More recently, back-projection methods or match field processing followed by noise source inversion have allowed better images of source distributions in the 3-10 s period band (e.g., Neale et al., 2017; Meschede et al., 2019; Retailleau and Gualtieri, 2019; Igel et al., 2023). Still, having a resolved knowledge of secondary microseismic noise source distribution from seismic data remains an issue with seismic stations mostly located on continents. Besides the problem of instrumental coverage, the regularization needed at least in source inversion also limits the resolution. Comparison between noise distribution from seismic data and spatially well-resolved numerical oceanic wave models shows satisfying similarities (e.g., Ardhuin et al., 2011; Stutzmann et al., 2012; Nishida and Takagi, 2022; Zhang et al., 2023), and long-time seismic data analysis could give feedback information to improve these models.

The WAVEWATCHIII (WW3DG, 2019) oceanographic hindcast model sub-product, computed by IFREMER (Ardhuin et al., 2011), allows comparison, with a default 3 hours resolution, to seismic data. Its accuracy has been evaluated in several studies and seismic application fields (e.g., Ardhuin et al., 2011; Stutzmann et al., 2012; Gualtieri et al., 2014; Farra et al., 2016; Tomasetto et al., 2024). However, using these models to compute seismic proxies, such as spectrograms (see the Appendix) or cross-correlations, requires knowledge of geophysics and ocean sciences. We present WMSAN for Wave Model Sources of Ambient Noise, a user-friendly Python package to help seismologists model their observations through maps of ambient noise sources from WW3 outputs, and also to compute spectrograms (e.g., Ardhuin et al., 2011; Stutzmann et al., 2012; Lecocq et al., 2020) and seismic noise correlations (Ermert et al., 2020).

Significant wave height, defined as the mean wave height of the third of the highest waves, should not be used as a proxy for seismic noise amplitude because the exact source mechanism has to be taken into account. We intend to physically describe seismic noise generation, considering bathymetry and wave-induced pressure close to the ocean surface. This package aims to be a useful tool for data analysis in ambient noise studies and to pave the way for further cooperation between seismology and oceanography. WMSAN will stay an open and collaborative package that aims to connect with other codes such as noisi (Ermert et al., 2020). For now, this package focuses exclusively on the secondary microseismic peak; however, other forcing, such as hum and primary microseisms, could also be implemented.

This report will first describe the main theory underpinning the WW3 products and how it can be used to build secondary microseism source maps, synthetic spectrograms, and synthetic cross-correlations. Then, detailed examples describe this package's applications. Table 1 summarizes the available outputs of the WMSAN package, their definitions, and illustrations in the following report. Each example described here can be found in a Jupyter Notebooks tutorial, and a summary of currently available notebook examples can be found in the Appendix Table 2. Details on the software accessibility, performance, and documentation can be found in the Data and Code Availability section, and the Appendix.

2 Theory: Secondary Microseisms Modeling

Secondary microseisms, or double-frequency microseisms, result from the non-linear interaction of ocean gravity wave trains of similar frequencies traveling in opposite directions. This interaction induces pressure changes close to the ocean surface, which generates seismic waves propagating within the Earth. Three configurations can lead to such a mechanism, described in Ardhuin et al. (2011). First, within a given storm, a steady wind generates waves in all directions interacting among themselves. Second, oceanic waves travel to the coast, are reflected, and interact with the incoming waves. Third, two ocean waves generated from different storms can propagate over long distances before interacting.

The WAVEWATCHIII (WW3) wave model is a state-of-the-art community-driven ocean wave hindcast, constrained by buoy and satellite data, integrating wave height, water depth, and surface current data. The WW3 hindcast model distributed by IFREMER (WW3DG, 2019) provides the pressure field at the sea surface from 1993 to 2022. The outputs include pressure sources resulting from the interaction of ocean wave coastal reflection with incoming waves, used for seismology applications (Ardhuin et al., 2011). We compute the transmission to the crust and the effect of bathymetry as amplification coefficients to obtain seismic source terms for the given seismic wave type.

This section explains the modeling of secondary microseismic sources for P, SV, and Rayleigh waves

Name	Unit	Symbol	Equation Number	Section	Figure	Output Format
Spectral density of the wave-induced pressure	$Pa^2.m^2.s$	F_P	(1)	2.1	-	NetCDF
Amplitude response functions of the Rayleigh waves modal decomposition	$\emptyset$	C	(2)	2.2	-	NetCDF
Amplification coefficient for body waves	$\emptyset$	$c_{P\|SV}$	(3)	2.2	-	NetCDF
Proxy of the source amplitude	N	F_{prox}	(4)	3.1	Figure 2 (Rayleigh, P, SV)	NetCDF (default) or hdf5 (noisi)
Equivalent Force	N	-	(5)	3.1	Figure 2	-
Source term for cross-correlation functions	$N^2.s$	S	(6)	3.2	Figure 4a	-
Synthetic Correlations	$\emptyset$ (normalized)	$\mathcal{C}$	(6)	3.1	Figure 4c	NetCDF
Power spectrum of the vertical displacement	m.s	S_{DF}	(7)	Appendix Rayleigh Waves Spectrograms	-	NetCDF
Power spectrum of the vertical ground displacement at a station	$m.s^{-1}$	F_δ	(8)	Appendix Rayleigh Waves Spectrograms	Figure Aa	-

Table 1 WMSAN available outputs names, symbols, equation number, section where it is defined and Figure where it is represented in this article.

from WW3 outputs and amplification coefficients at the source location, considering a 2-layer medium (ocean and crust) and ignoring the sedimentary layer.

2.1 Spectral Density of the Wave Induced Pressure

We follow the notation from Farra et al. (2016) in this section. The secondary microseismic source computation first depends on the directional wave spectrum $F(\mathbf{r}, f, \theta) = E(\mathbf{r}, f)M(\mathbf{r}, f, \theta)$, where the power spectrum of the vertical sea surface displacement $E(\mathbf{r}, f)$ is punctually given by buoy and satellite data, and $M(\mathbf{r}, f, \theta)$ gives the directional distribution of elevation for each frequency. Then the spectral density of the wave-induced pressure just below the sea surface F_p, in $Pa^2.m^2.s$ is computed as:

$$F_p(\mathbf{r}, 2f) = [2\pi]^2[\rho_w g]^2 2f E^2(\mathbf{r}, f) \int_0^\pi M(\mathbf{r}, f, \theta)M(\mathbf{r}, f, \theta + \pi)d\theta \tag{1}$$

where $\mathbf{r}$ is the 2D coordinate vector, ρ_w is the density of water, g the standard acceleration of gravity, f the oceanic wave frequency, and θ the ocean gravity wave direction angle.

The significant wave height (H_s), defined as : $H_s(\mathbf{r}) = 4\sqrt{\int_0^\infty E(\mathbf{r}, f)df}$, carries no information about the direction of the oceanic waves and therefore no information about interactions between opposite oceanic wave trains. This leads to our emphasis on using the spectral density of the wave-induced pressure just below the sea surface F_p for seismic sources modeling, as emphasized in Ardhuin et al. (2011).

F_p is directly given as a WW3 output (WW3DG, 2019); therefore, WMSAN depends on the availability of these files (from 1993 to 2022 presently). We provide a Python library that reads and transforms F_p into products easily useable by seismologists. Now that the wave-induced pressure is known, we focus on energy transmission to the crust by computing bathymetry effects for a given seismic wave type.

2.2 Site Effects or Amplification Coefficients

Site effects, or amplification coefficients, act as a spatial amplitude modulator in the source computation. The ocean acoustic wave generated by secondary microseismic sources transmission to the crust might differ depending on the seismic frequency and incident angle. Kedar et al. (2008); Ardhuin et al. (2011); Stutzmann et al. (2012); Gualtieri et al. (2013, 2014) extensively described how site effects can be computed for Rayleigh waves using surface wave modal decomposition and for body waves using plane wave approximation. In the following paragraphs, we recall how these coefficients are calculated following Gualtieri et al. (2014) and Longuet-Higgins (1950) for body and Rayleigh waves, respectively. Let us note that we only focus on vertical motion transmission to the seafloor, so SH and Love waves are not taken into account here but have been observed and discussed in previous studies (e.g. Nishida and Takagi, 2016; Juretzek and Hadziioannou, 2016; Ziane and Hadziioannou, 2019; Gualtieri et al., 2020, 2021).

Secondary microseismic ambient noise records are dominated by surface waves which are therefore widely used for imaging local to regional areas or monitoring (e.g., Sabra et al., 2005; Bensen et al., 2008; Lu et al., 2018), so modeling Rayleigh wave generation has been an extensive field (Kedar et al., 2008; Ardhuin et al., 2011; Stutzmann et al., 2012; Gualtieri et al., 2014; Gimbert and Tsai, 2015). As in Gualtieri et al. (2013) a surface wave modal representation of the elastic displacement field is widespread in the literature: in particular, the fundamental mode for Rayleigh waves predominates the signal. We follow Longuet-Higgins (1950) tables to compute the amplitude response functions of the Rayleigh wave modal decomposition, for the case of a pressure source close to the ocean surface and a receiver at the ocean bottom, in a 2 layer model composed of the ocean, of given thickness h, and a crustal half space, as:

$$C(f_s, h) = \sum_{i=1}^{4} c_i^2(f_s, h) \tag{2}$$

where h is the water column depth, $f_s = 2f$ the seismic frequency, and f the ocean frequency in Hz. c_i is the Rayleigh wave amplitude response function for the mode number i. Longuet-Higgins (1950) tables go from 1 to 4, where $i = 1$ is the fundamental mode. This simple approach could be improved in future package versions by recomputing the c_i coefficients with different medium velocities and densities, and also including sedimentary layers effects as in Gimbert and Tsai (2015). For more accurate modeling of surface waves, see Xu et al. (2025), which accounts for the source and receiver site effects separately, including the sediment layer.

For body waves, assuming a plane wave traveling in the water layer and transmitted to the crust, therefore neglecting the sediment layer, the amplification coefficient for body waves is given by Gualtieri et al. (2014) as follows:

$$c_{P\ |SV}(f_s, h) = \sqrt{\int_0^{\theta^*_{P_w}} \left| \frac{T_{P|SV}(\theta_{P_w})}{1 + R(\theta_{P_w}) \exp^{i\phi_w(h(\mathbf{r}), 2\pi f_s, \theta_{P_w})}} \right|^2 d\theta_{P_w}} \tag{3}$$

where h is the ocean depth, θ_{P_w} (default critical angle 15.71°) the P or SV-wave takeoff angle range ($P \mid SV$), ϕ_w the plane P/SV-wave potential propagating in water, R the seabed interface reflection coefficient, and $T_{P/SV}$ the seabed interface P or SV wave transmission coefficient. The body wave amplification depends on the P-wave incident angle at the source, θ_{P_w} (Farra et al., 2016). Here we consider a proxy of this amplification by integrating over all angles which enables us to have a single coefficient for each source location. The takeoff angles higher than 15.71° are not accounted for since R and $T_{P/SV}$ coefficients become complex, and we are not interested in evanescent waves (Gualtieri et al., 2014). The sediment layer is negligible if its thickness is lower than half the wavelength of the studied seismic waves, which is the case in most oceans in the 3-10s period band,≤ 6 km (Straume et al., 2019).

Once the spectral density of the wave-induced pressure in the ocean layer and the site effect at the seafloor interface is defined, we introduce default examples to compare observed data to synthetic counterparts based on WW3 ambient noise source distribution.

3 WMSAN to Compute Sources, Synthetic Cross-Correlations and Spectrograms, Based on Ocean Wave Models

Useful outputs of the WW3 hindcast to seismologists are the spectral density of the induced wave pressure (p2l) and bathymetry files, saved in NetCDF format. Each of these products can be found on the IFREMER ftp ftp://ftp.ifremer.fr/ifremer/ww3/HINDCAST/SISMO/ (e.g., Ardhuin et al., 2011). The grid used by default in the package has a 0.5° resolution in both latitude (ranging from 78°S to 80°N) and longitude (from 180° W to 179.5° E). It spans 22 frequencies from 0.08 Hz to 0.61 Hz with a 3-hour time step from 1993 to 2022.

WMSAN only provides tools to model seismic data proxies, such as synthetic spectrograms, synthetic cross-correlation, or maps of the distribution of seismic sources. We do not provide tools to handle recorded seismic data, since other Python packages can be used for data processing such as ObsPy (e.g., Krischer et al., 2015) or, more specifically for ambient noise studies, to calculate cross-correlations such as MSNoise or NoisePy (e.g., Lecocq et al., 2014; Jiang and Denolle, 2020).

Alternatively, one may recompute the wave-induced pressure from the full directional spectra archived by the European Center for Medium-range Weather Forecasting (ECMWF); either in their operational analysis and forecasts or in reanalyses such as ERA5 (e.g., Hersbach et al., 2020). The ECMWF wave spectra do not include coastal reflections and use slightly different parameterization, resulting in different spectral shapes and wave-induced pressure levels.

Figure 1 is a diagram describing the different outputs of the package and how they connect in addition to Table 1. Six different outputs are available in this package: the site effect computation on refined grids; surface wave synthetic spectrograms as computed in Ardhuin et al. (2011) and Stutzmann et al. (2012); source maps including amplification coefficients effect; temporal variations for the source in a given area; and synthetic auto- and cross-correlations. Square boxes represent external entities used as inputs, we denote the WW3 spectral density of the pressure field (F_p) and the bathymetry used to compute the previously described site effects. One can either use the default bathymetry or use a finer grid such as the 1 arc min resolution given by the ETOPO Global Relief Model (NOAA National Centers for Environmental Information, 2022). Specific grids such as the coast of Africa or New Caledonia are also available. Each external element is used to compute the Rayleigh waves synthetic spectrograms (details in the Appendix)

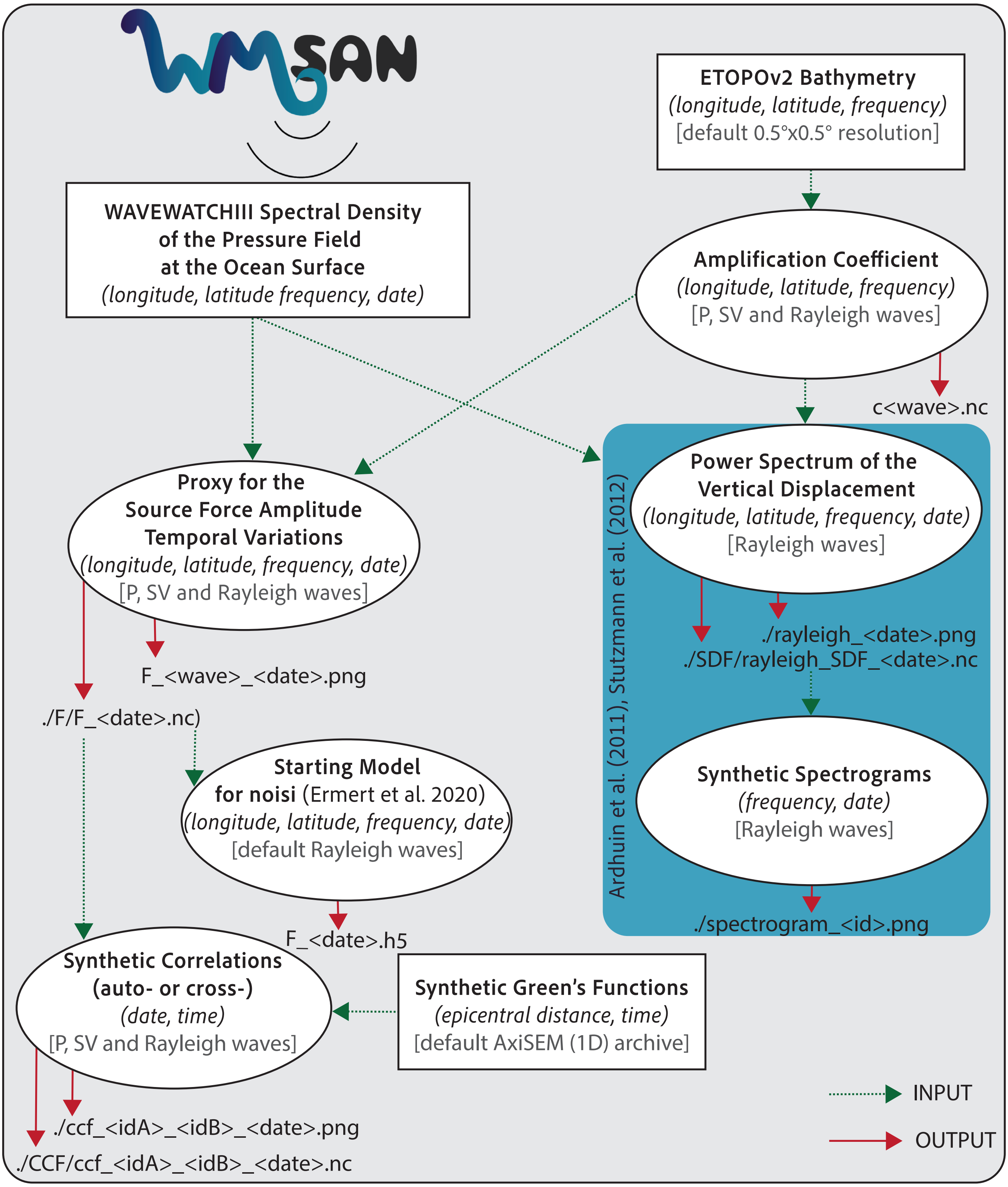

Figure 1 Diagram representation of the different products available in WMSAN and their interactions. Green dotted line arrows represent the input dataset to provide to the package functions, some are given by default. Red plain arrows represent each function's default output file names and format.

but also body and Rayleigh waves' source maps and synthetic correlations. The outputs are stored in NetCDF format (UCAR/Unidata) by default, or in HDF5 format for the starting model for noisi (The HDF Group).

3.1 Source Maps: Proxy for the Source Amplitude

Sources are computed on the whole ocean's surface grid provided by WW3 as the amplitude of the vertical force applied on the sea surface modulated by the previously described site effect, as described in previous studies (Zhang et al., 2023; Boué and Tomasetto, 2024; Tomasetto et al., 2024). This proxy for the source is an estimation of the effective force amplitude using a proxy for the source site effect. Each site effect relies on different assumptions: normal mode summation for Rayleigh waves, and plane wave approximation for body waves. Therefore, this proxy should not be interpreted as the vertical force applying on the seafloor, but as an approximation for the source distribution. We define this proxy of the source amplitude as F_{prox} (in N) as:

$$F_{\text{prox}}|_i(\mathbf{r}) = 2\pi\sqrt{\int_{f_{s_{min}}}^{f_{s_{max}}} c^2(\mathbf{r}, f_s) F_p|_i(\mathbf{r}, f_s, \mathbf{K} \approx 0) dA df_s} \tag{4}$$

where i is the date step with a 3-hr resolution, $\mathbf{r}$ the location on the grid, $dA = R^2 cos(\lambda) d\lambda d\phi$ the cell surface element, R the Earth's radius, λ the latitude, and ϕ the longitude. The c symbol denotes the site effect of the wave type of interest: for body waves, we use $c_{P/SV}(f_s, h)$, and for Rayleigh waves, $\sqrt{C(f_s, h)}$, as described in equations 2 and 3 respectively. The corresponding Jupyter Notebooks for Rayleigh waves and body waves can be found in **/notebooks/rayleigh_waves/microseismic_sources.ipynb** and **/notebooks/body_waves/microseismic_sources.ipynb** respectively. The custom site effect can be computed for Rayleigh waves, corresponding to the functions used in the Jupyter Notebook entitled **/notebooks/rayleigh_waves/amplification_coefficients.ipynb**. Similarly, an estimate of body waves' site effect (P and SV) can be computed for a given bathymetry using the Jupyter Notebook entitled **/notebooks/body_waves/amplification_coefficients.ipynb**.

Figure 2 shows an example of the resulting maps for each type of seismic wave during the first three Mondays (05, 12, and 19) of January 2014. The top row presents the equivalent force which is defined similarly to F_{prox} without amplification coefficients applied:

$$\text{Equivalent Force} = 2\pi\sqrt{\int F_p|_i(\mathbf{r}, f_s, \mathbf{K} \approx 0) df_s dA} \tag{5}$$

As pointed out by Gualtieri et al. (2014), P-waves are more amplified than SV-waves, which might explain why the latter are rarely observed in the 3-10s period band (Nishida and Takagi, 2016). Also, the distribution of noise sources is typical for this season, with stronger sources in the Northern Hemisphere from October to March, and stronger sources in the Southern Hemisphere from April to September. Rayleigh waves are enhanced within smaller and sharper-edged areas than their body wave counterparts. The Rayleigh wave amplitude appears between P and SV wave levels. These maps can be used either to visualize the spatiotemporal distribution of secondary microseisms, or to compare to back-projection (e.g., Retailleau and Gualtieri, 2021) and source inversion results (Igel et al., 2021, 2023). The package allows saving these maps as matrices, with both spatial and frequency dimensions, to be used as an input to build synthetic cross-correlations (see Figure 1).

3.2 Synthetic Cross-Correlations Implementation

The seismic interferometry founding principle relies on the correlation operator between two seismic recordings to extract or enhance coherency hidden in continuous oscillations. Seismic noise records have been used for many applications, including monitoring the spatio-temporal evolution of the crust and the subsurface, and seismic imaging at different scales. This has opened the possibility to supplement the information provided by earthquakes, (e.g., Shapiro et al., 2005). Two different interpretations of cross-correlations can be distinguished. The first, more widespread, assumes that noise correlations provide the Green's function between two sensors, but depends on strong assumptions such as wavefield equipartition or homogeneous distribution of noise sources (e.g., Weaver and Lobkis, 2002; Sanchez-Sesma and Campillo, 2006; Wapenaar and Fokkema, 2006). The second one considers cross-correlation without assuming that it corresponds to Green's function of the medium, as a differential measure of wave propagation (e.g., Sager et al., 2021). The latter do not rely on strong assumptions but require estimating the source spatio-temporal evolution to deduce information on the sampled medium. The WMSAN package aims to provide a convenient way to model oceanic noise sources and compute synthetic correlations.

Figure 3 shows the data flow to compute synthetics cross-correlation between vertical components, as in Ermert et al. (2020) and Tomasetto et al. (2024). Using the representation theorem and assuming temporally uncorrelated source points (e.g., Wapenaar and Fokkema, 2006), one can write the cross-correlation function between sensors A and B as:

$$\begin{aligned} &\mathcal{C}(\mathbf{r}_A, \mathbf{r}_B, t) \\ &= \mathcal{FT}^{-1}\left[\int_{\partial D} G(\mathbf{r}_A, \mathbf{r}, f_s) G^*(\mathbf{r}_B, \mathbf{r}, f_s) S(\mathbf{r}, f_s) dr\right] \end{aligned} \tag{6}$$

with $G(\mathbf{r}_A, \mathbf{r}, f_s)$ the Green's function between a source in $\mathbf{r}$ and station A in $\mathbf{r}_A$. The star symbol * denotes the complex conjugate and ∂D the spatial domain of potential sources, here the ocean's surface. The inverse Fourier transform is written as $\mathcal{FT}^{-1}$. The source term $S(\mathbf{r}, f_s) = 4\pi^2 C(\mathbf{r}, f_s) F_p|_i(\mathbf{r}, f_s, \mathbf{K} \approx 0) dA$ represents a proxy of the source PSD at the horizontal position $\mathbf{r}$, given by the square of proxy for the source amplitude for Rayleigh waves. Therefore, we do not expect to retrieve the absolute amplitude of the real data cross-correlation, but rather a first estimate of the relative amplitude variability as a function of source distribution and frequency content. The assumption of temporally uncorrelated sources relies on the fact that the source grid has a 0.5° step in both latitude and longitude, so the sea state variations between two adjacent grid points appear uncorrelated. Also, in the case of temporally correlated sources, cross-correlations show repeating patterns and spurious arrivals (e.g., Schippkus et al., 2023), which doesn't seem observed in most examples in the secondary microseismic band.

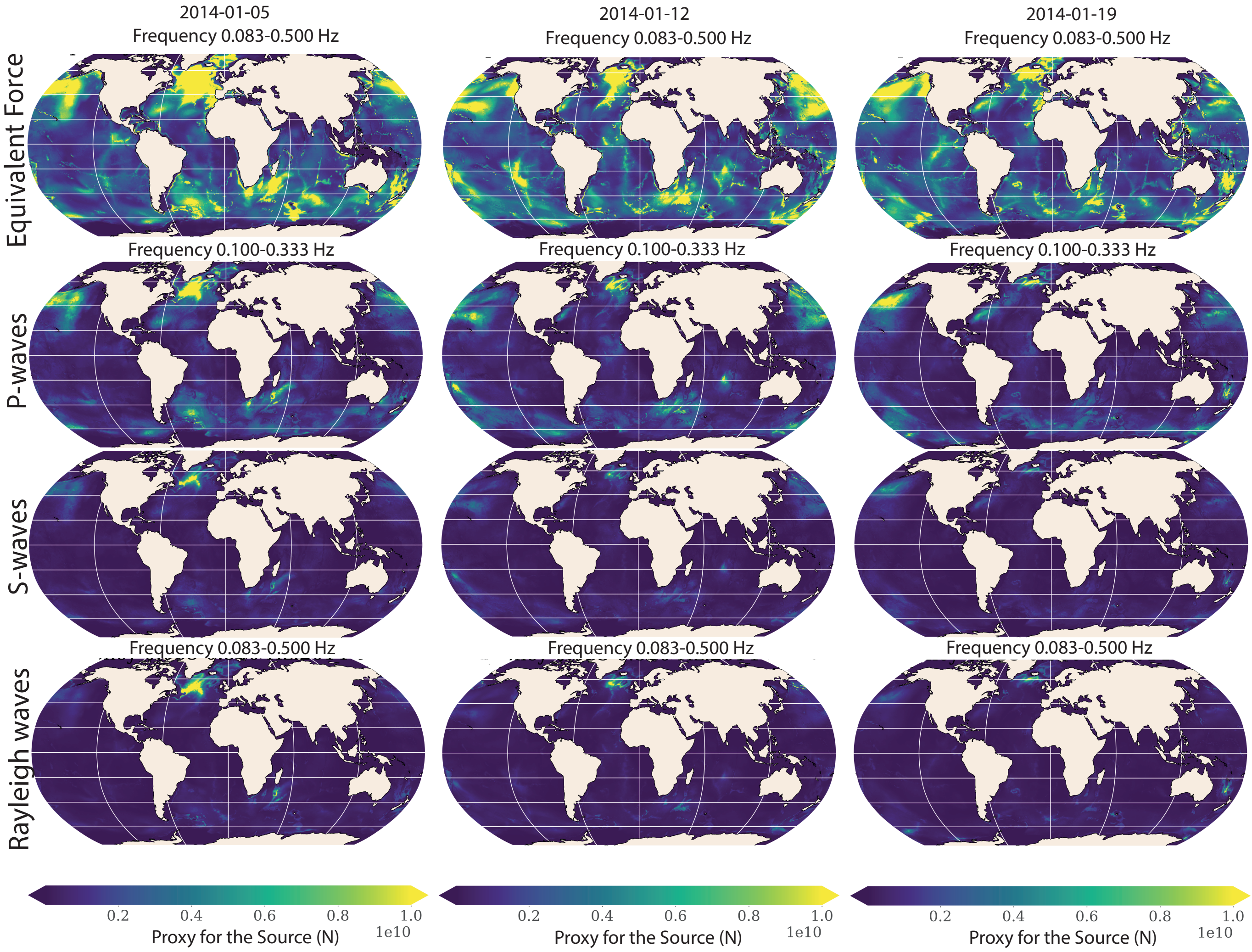

Figure 2 The standard output of WMSAN compared to the equivalent force (top row) without site effect modulation. The proxy for the source amplitude (F) the first three Mondays of January 2014, for P-waves (second row), SV-waves (third row), and Rayleigh-waves (bottom row).

Here, Green's functions are computed in an axisymmetric laterally invariant Earth model using AxiSEM (Nissen-Meyer et al., 2014), which does not include the ocean fluid layer. Since we intend specifically to model Rayleigh waves, we window surface waves and discard other arrivals. This prevents the contribution of cross-term. Also, we do not observe other significant interferences in the example below, which can be explained by incoherent noise in the records or instrumental threshold for detection. Also, the Green's Functions used are computed with laterally averaged attenuation and dispersion, therefore we illustrate a simple case in the following section by only focusing on a homogeneous area for wave propagation. The corresponding Jupyter Notebook can be found in **/notebooks/rayleigh_waves/synthetic_CCF.ipynb**.

This package only provides the possibility to compute synthetic cross-correlations in a spherically symmetric model. To compute more realistic cross-correlations in 3D models we suggest the user run noisi (Ermert et al., 2020). A function to link both packages is available to use the WMSAN output as a starting model for noisi as shown in Figure 3. WMSAN provides a function to taper specific phases in the Green's function archive, which is not the case in noisi, therefore our package might be useful to focus on specific body wave phase interferences (PP-P, see **/notebooks/body_waves/synthetic_CCF.ipynb**).

3.3 Example for a Single Station Pair

Next, we show that the transit of a storm for a few days generates Rayleigh waves and how wave models can help us understand waveform variations in cross-correlation functions.

We focus on 6 days from 14 to 20 November 2014, during which a strong source occurred in Northern Iceland in the North Atlantic that we selected from Nishida and Takagi (2022) catalogs. We pick two seismic stations from the LAPNET network in northern Finland (Kozlovskaya, 2007), XK.LP51.00 and XK.SGF.00 whose inter-station path is oriented towards the source area. The LAPNET network has been used in previous studies to detect P-waves from secondary microseismic sources (Poli et al., 2012a; Boué et al., 2013) and is located on the Northern Baltic shield known to have a quite homogeneous crust (Poli et al., 2012b), leading to the relevant use of laterally uniform Earth models Green's func-

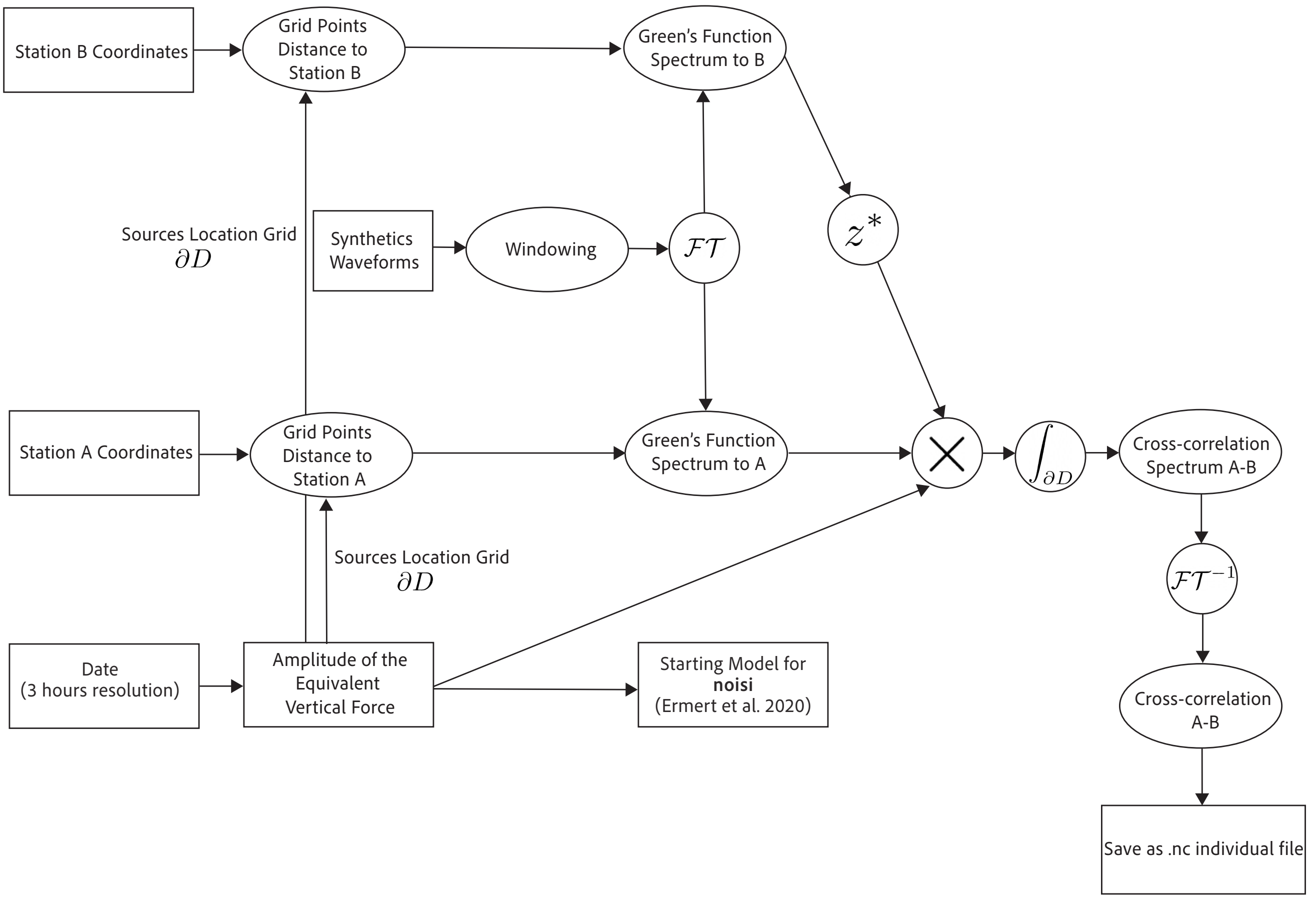

Figure 3 Data flow representing synthetics computation script. Based on representation theorem formulation (Aki and Richards, 2002; Nakata et al., 2019).

tions (ak135f). The package is built to be adjustable, so one could also use Green's Functions computed in a different model as input, for example, computed with AxiSEM (Nissen-Meyer et al., 2014). Other synthetic seismogram software, such as instaseis (van Driel et al., 2015), are not yet implemented with the package but can be used via noisi (Ermert et al., 2020).

Figure 4a shows the proxy for the source force amplitude, including Rayleigh waves site effect, summed over 14-20 November 2008 computed as previously described and the two stations' locations. Equation 6 depends on the source PSD and Green's Functions between each potential source point, imposed by the wave model grid. We use AxiSEM precomputed Green's Functions in ak135f model with PREM attenuation (Kennett et al., 1995; Dziewonski and Anderson, 1981), sampled at 1Hz propagating for 3600 s for a vertical point force of 10^{20} N, shown in Figure 4b. Figure 4b shows the distance-time Green's functions waveforms used, which has a 0.1° distance sampling. The red and green lines depict velocities of 4.2 km/s and 2.5 km/s respectively, used for the Green's Function tapering.

Synthetic cross-correlations with site effect modulation (left) are computed every 3 hours and compared to their data counterpart (right) in Figure 4c). The figure shows causal and acausal parts of the cross-correlations normalized by the maximum value over the whole panel to highlight the amplitude variations. No particular post-processing has been done to remove earthquakes; we present raw cross-correlations. The maximum amplitudes appear from the 18th of November at noon to the 19^{th} at noon with site effect modulation, matching the data amplitude variations. Rayleigh waves' arrival times correspond for both synthetic and data, around 35 s on the causal part (from KP51 to SGF), which is explained by the homogeneous medium sampled, the East European Craton. Synthetic cross-correlation without site effect can be computed, and shows less amplitude contrast than its site effect modulated counterpart, but its maximum amplitude around midnight on the 18th of November differs from the data. The comparison between cross-correlation without site effect, with site effect, and the data is available in the Appendix section in Figure B.

Some notable discrepancies between waveforms remain, such as the variations in amplitude on the 16^{th} of November related to the source modeling, or the main pulse's frequency content. The data is filtered in the 2-10 s period band, similar to the discrete frequency range of the WW3 model (from 0.08 Hz to 0.61 Hz). Recent developments in wave modeling parameters by Alday and Ardhuin (2023) using confirmation from infrasound data can improve the accuracy for frequencies above 0.4 Hz. Figure 4c shows the spatiotemporal evolution of the retrieved surface wave with variations of tens of seconds in a few hours, so this tool can help discriminate source from propagation contributions and therefore deduce structural effects. One can also discrimi-

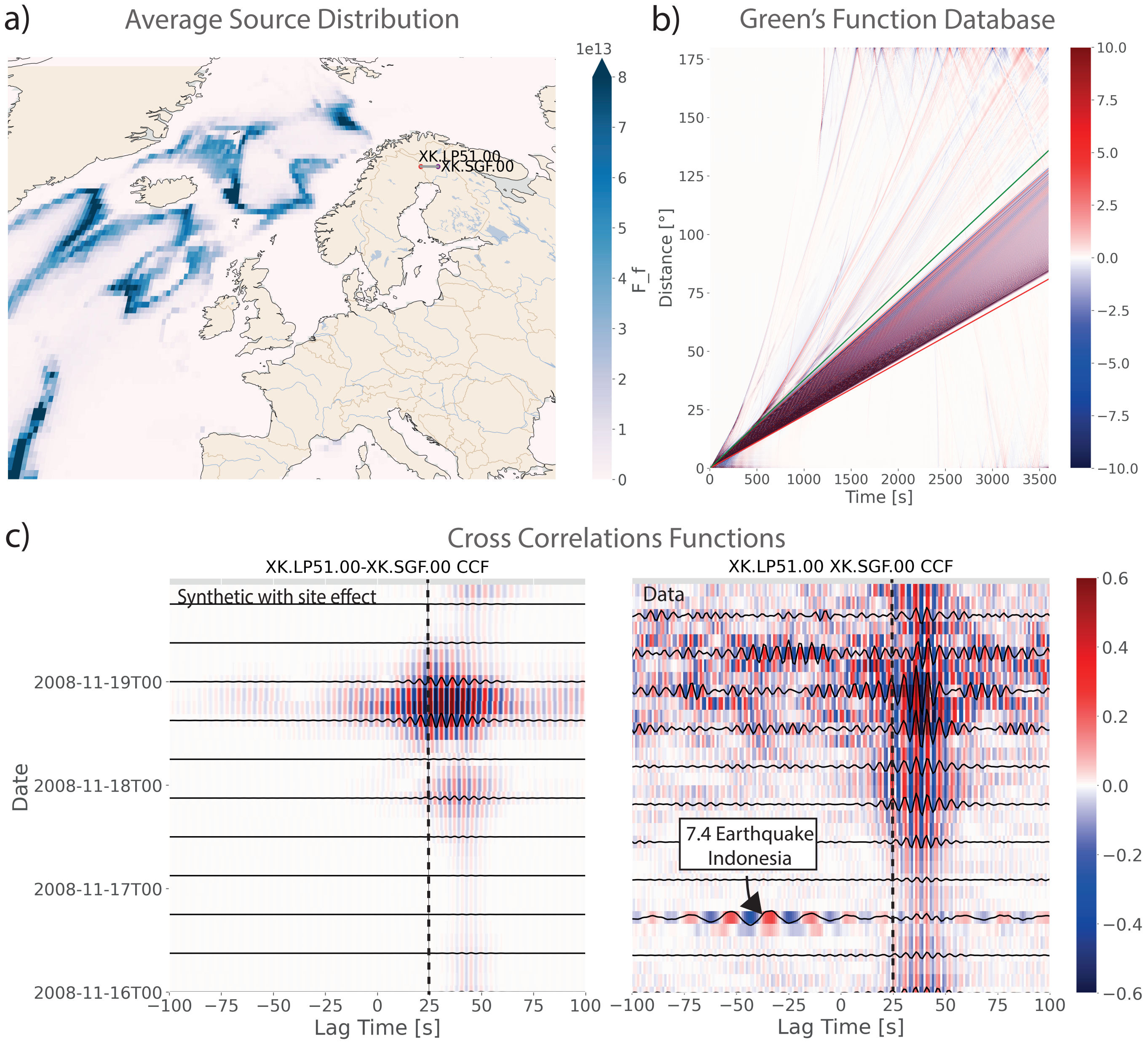

Figure 4 a) Station pair (XK.LP51-XK.SGF) used from the LAPNET network (XK) (Kozlovskaya, 2007) and the source distribution from 14-20 November 2008. b) Synthetic Green's Functions used in the cross-correlation modeling. c) Cross-correlations functions from 16-20 November 2008 split into 3 hr windows. Waveforms normalized by the maximum value of the panel. (left) Synthetic cross-correlation functions with site effect modulation, (right) Data-based cross-correlation functions.

nate other sources, for example, a long-period signal is seen in the data on the 16th of November 2008 in the 3-6 p.m. segment, corresponding to a Mw 7.4 teleseismic earthquake in Minhassa Peninsula, Indonesia. Given these points, the medium information present in the data should be the main origin of waveform mismatch. One can imagine improving the modeling using a well-resolved 3D model of the studied area.

Finally, this simple modeling can help understand the source spatiotemporal impact on cross-correlations, consequently partly removing uncertainties on the cross-correlations features.

4 Conclusion

We presented the WMSAN Python package, a user-friendly Python library to compute proxy for ambient noise source maps, synthetic spectrograms (see the Appendix), and simple synthetic correlation functions to compare to data counterparts. We hope this tool can help improve collaboration between seismologists and oceanographers, and incite the use of WW3 spectral density of the pressure field at the sea surface instead of significant wave height in seismology studies. To help the user get started with the package, we provide an ensemble of Jupyter Notebooks, detailing the previously described examples. A list of the available notebooks is given in the Appendix, as well as links to the library's `documentation`. This tool answers a need in the community to comprehend the source distribution of sec-

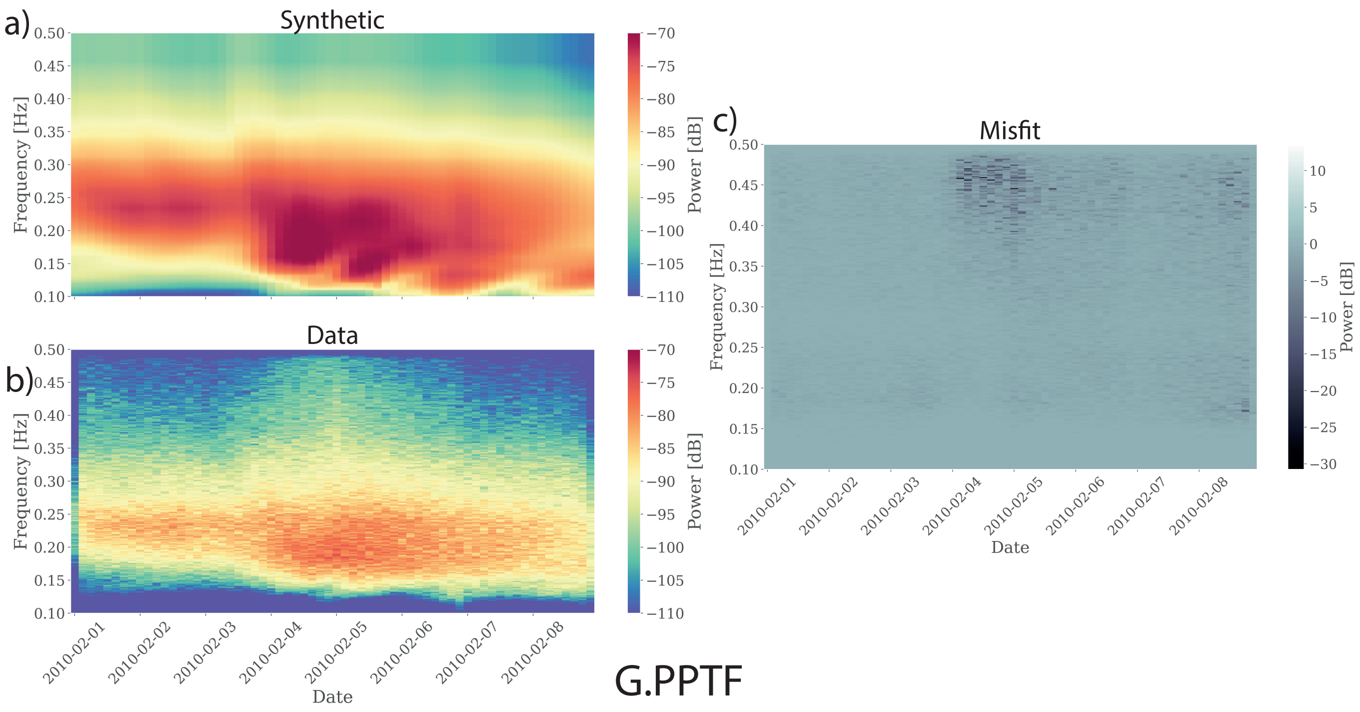

Figure A a) Interpolated synthetic spectrograms with propagation effect coefficient $P(f_s) = 1.9$, and b) data-based spectrograms of stations G.PPTF 1-9 February 2010. c) Misfit between synthetic and data spectrograms as defined in Stutzmann et al. (2012).

ondary microseisms. We also believe oceanographers and climate scientists can use these tools to extract information on past oceanic events from seismic data, and even study past climate (e.g., Aster et al., 2023). We support any comments or contributions to improve future versions of this open-source package.

Acknowledgements

This research was funded by the French National Research Agency (ANR) under the project TERRACORR (ANR-20-CE49-0003). We thank Paula Koelemeijer, the editor, and two anonymous reviewers for their insightful comments that greatly improved this manuscript.

The authors would like to thank Mickael Accensi who produced the WW3 outputs and teaches how to run WAVEWATCHIII every year in a summer school in Brest, France. We are grateful for the help Laura Ermert provided to link noisi to WMSAN. We also would like to thank all the people who gave feedback during the development of this package: Lalit Arya, Reza D. D. Esfahani, Rémy Monville, Clément Robert, Adrien Soudais, and Yixiao Sheng.

We also thank all technical staff and institutions for allowing seismic and oceanic data to be distributed globally.

Data and Code Availability

Full documentation for the WMSAN library as well as the examples used in this paper are available on a dedicated page: https://tomasetl.gricad-pages.univ-grenoble-alpes.fr/ww3-source-maps/. This code is available on the Université Grenoble Alpes' GitLab repository: https://gricad-gitlab.univ-grenoble-alpes.fr/tomasetl/ww3-source-maps. It is also mirrored on Lisa Tomasetto's personal `GitHub` repository. Hosting on `Zenodo` is available, as well as the ETOPO bathymetry file and AxiSEM waveforms database in a separate repository https://zenodo.org/records/11126562. The Python library is also distributed on `PyPI`. It is an open-source library, any contribution or suggestion is welcome.

Competing Interests

The authors have no known competing interests.

Appendix

Rayleigh Waves Spectrograms

We compute spectrograms using equations given by Ardhuin et al. (2011). Stutzmann et al. (2012) highlighted that an additional parameter $P(f_s)$ representing the three-dimensional (3D) propagation effects might be needed to model spectrograms for stations located on islands or near the poles, where ice layer-induced variations are poorly modeled. We added this parameter as an option; however, a package based on Stutzmann et al. (2012) will be published later by the original authors where they adjust the ocean wave coastal reflection and attenuation factor for each station (Xu et al., 2025). The GitLab repository of the WMSAN project will redirect to the second code as soon as it is available, and we invite any user to compare and test both packages. Lecocq et al. (2020) used similar analog spectrograms' computation using WW3 hindcast to validate extreme

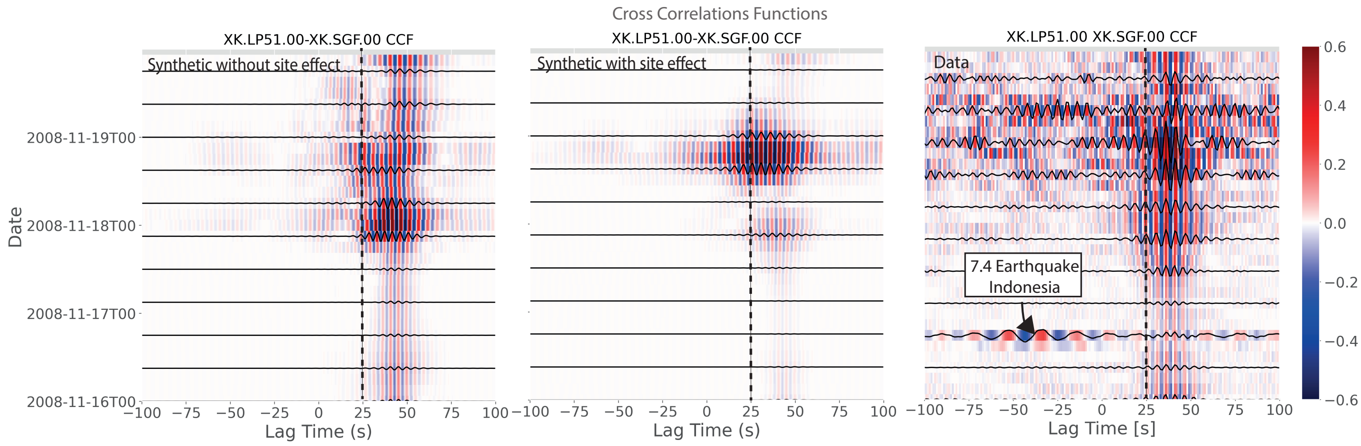

Figure B Cross-correlations functions of station pair (XK.LP51-XK.SGF) from 16-20 November 2008 split into 3 hr windows. Waveforms normalized by the maximum value of the panel. (left) Synthetic cross-correlation functions without site effect modulation (middle) Synthetic cross-correlation functions with site effect modulation, (right) Data-based cross-correlation functions.

floods events in Belgium.

We first compute the equivalent source of the power spectrum of the vertical displacement $S_{DF}(f_s)$ in m.s, corresponding to the Jupyter Notebook **/notebooks/rayleigh_waves/rayleigh_source**.ipynb, and defined as:

$$S_{DF}(f_s) \approx \frac{2\pi f_s C(f_s, h)}{\rho_s^2 \beta^5} F_p(f_s) \tag{7}$$

with f_s the seismic frequency in Hz, C the amplitude response functions for the normal modes previously described (site effect), ρ_s the rock density, and β the shear wave velocity. We then calculate the power spectrum of the vertical ground displacement at a station of latitude λ and longitude ϕ in m^2.s^{-1}:

$$F_\delta(\lambda, \phi, f_s) \tag{8}$$
$$= \int_{-\pi/2}^{\pi/2} \int_0^{2\pi} \frac{S_{DF}(f_s)}{R_E sin\Delta} P(f_s) e^{-2\pi f_s \Delta R_E/(UQ)} R_E^2 \cos\phi' d\lambda' d\phi'$$

with Q the dissipation quality factor, $P(f_s)$ the 3D propagation effect coefficient, Δ the distance between source and station in radians, R_E the Earth's Radius in meters, and U the group velocity of Rayleigh waves in m.s^{-1}. The corresponding Jupyter Notebook is **/notebooks/rayleigh_waves/spectrograms**.ipynb.

We plot the modeled spectrogram at each time step of the model (default 3-hour resolution) as:

$$S_{spectrogram}(f_s) = 10log_{10}(\sqrt{F_\delta(\lambda, \phi, f_s)})$$

An example of synthetic spectrograms is shown in Figure A (a) compared to the equivalent data spectrogram (b) filtered between 0.1Hz and 0.5Hz for PPTF station from the GEOSCOPE network from 1-9 February 2010 (GEOSCOPE, French Global Network of broad band seismic stations, 1982). We took the values given in Stutzmann et al. (2012) for the different parameters, such that $Q = 450$, $P = 1.9$, $U = 1800\,\text{m.s}^{-1}$, $\rho_s = 2600\,\text{kg.m}^{-3}$, and $\beta = 2800\text{m.s}^{-1}$. The synthetic spectrogram seems to overestimate amplitudes compared to real data. This might be due to the three-dimensional wave propagation that is poorly constrained here (constant attenuation factor with distance). Note that the wave model used for this simulation may differ from the older wave model restricted to 0.1-0.3 Hz used by Stutzmann et al. (2012). We introduce a misfit measure from Stutzmann et al. (2012) that allows the user to compare synthetic and data quantitatively, as shown in Figure Ac. In the PPTF example, the discrepancies in amplitude are visible in the 0.4-0.5 Hz band, as well as punctual bursts at low frequencies.

Comparison of the Site Effect Impact On Cross-correlation Functions

Synthetic cross-correlation without site effect can be computed by replacing the amplification coefficient input with a matrix filled with ones. Figure B shows the comparison between modeled cross-correlation functions without (left) and with (middle) site effect. The data cross-correlations are shown in the right panel. The modeling without site effect shows less amplitude contrasts than its site effect modulated counterpart highlighting the arrival at 40 s. However, its maximum amplitude around midnight on the 18th of November differs from the data.

Corresponding Jupyter Notebooks

Table 2 summarizes the possible values to compute and which Jupyter Notebooks to run to reproduce the figures shown in this article. Numbers indicate in which order to run Notebooks for the synthetic spectrograms and cross-correlation functions cases.

Python Functions Performance

Table 3 gives the run time of the main functions in each Jupyter Notebook, illustrating the formerly detailed examples.

Object to Compute	Jupyter Notebook Path	Figure
Amplification Coefficient (body waves)	/notebooks/body_waves/amplification_coefficients.ipynb	-
Amplification Coefficient (Rayleigh waves)	/notebooks/rayleigh_waves/amplification_coefficients.ipynb	-
Proxy for the Source Force Amplitude (body waves)	/notebooks/body_waves/microseismic_sources.ipynb	Figure 2
Proxy for the Source Force Amplitude (Rayleigh waves)	/notebooks/rayleigh_waves/microseismic_sources.ipynb	Figure 2
Spectrograms (Rayleigh waves)	1) /notebooks/rayleigh_waves/rayleigh_sources.ipynb 2) /notebooks/rayleigh_waves/spectrogram.ipynb	Figure A
Synthetic Cross-correlations (Rayleigh waves)	1) /notebooks/rayleigh_waves/microseismic_sources.ipynb 2) /notebooks/rayleigh_waves/synthetic_CCF.ipynb or 2) /notebooks/rayleigh_waves/wmsan_to_noisi.ipynb	Figure 4

Table 2 Table summing up the directory where each example of WMSAN can be found and in what order.

Object	Notebook	Function	Runtime
Download WW3 Files	Several	subfunctions_rayleigh_waves. download_ww3_local	15 min per monthly file
Site effect (body waves)	amplification_coefficient.ipynb	subfunctions_body_waves.ampli	10^{-3}s per gridpoint
(Rayleigh waves)	amplification_coefficient.ipynb	subfunctions_rayleigh_waves.site_effect	10^{-5}s per gridpoint
Force Maps	microseismic_sources.ipynb	subfunctions_rayleigh_waves.loop_WW3	10s per day
Temporal Variations	temporal_variations.ipynb	temporal_variation.temporal_evolution	14s per month
SDF Spectrogram	rayleigh_source.ipynb	subfunctions_rayleigh_waves.loop_SDF	44s per day
Synthetic Correlations Rayleigh and Body waves	synthetic_CCF.ipynb	synthetics.compute_ccf	4.10^{-3}s per grid cell per timestep
Auto-correlation	synthetic_CCF_autocorr.ipynb	synthetics.compute_ccf_autocorr	5.10^{-3}s per grid cell per timestep

Table 3 Performances in terms of the run time of the main functions in each Jupyter Notebook provided as examples.

References

Aki, K. and Richards, P. G. *Quantitative seismology*. Cambridge University Press, 2002.

Alday, M. and Ardhuin, F. On Consistent Parameterizations for Both Dominant Wind-Waves and Spectral Tail Directionality. *Journal of Geophysical Research: Oceans*, 128(4):e2022JC019581, 2023.

Ardhuin, F. Large-scale forces under surface gravity waves at a wavy bottom: A mechanism for the generation of primary microseisms. *Geophysical Research Letters*, 45(16):8173–8181, 2018.

Ardhuin, F., Stutzmann, E., Schimmel, M., and Mangeney, A. Ocean wave sources of seismic noise. *Journal of Geophysical Research*, 116(C9):C09004, Sept. 2011. doi: 10.1029/2011JC006952.

Ardhuin, F., Gualtieri, L., and Stutzmann, E. How ocean waves rock the Earth: Two mechanisms explain microseisms with periods 3 to 300 s. *Geophysical Research Letters*, 42(3):765–772, Feb. 2015. doi: 10.1002/2014GL062782.

Ardhuin, F., Stopa, J. E., Chapron, B., Collard, F., Husson, R., Jensen, R. E., Johannessen, J., Mouche, A., Passaro, M., Quartly, G. D., et al. Observing sea states. *Frontiers in Marine Science*, 6:124, 2019.

Aster, R. C., Ringler, A. T., Anthony, R. E., and Lee, T. A. Increasing ocean wave energy observed in Earth's seismic wavefield since the late 20th century. *Nature Communications*, 14(1):6984, Nov. 2023. doi: 10.1038/s41467-023-42673-w.

Bensen, G., Ritzwoller, M., Barmin, M., Levshin, A. L., Lin, F., Moschetti, M., Shapiro, N., and Yang, Y. Processing seismic ambient noise data to obtain reliable broad-band surface wave dispersion measurements. *Geophysical journal international*, 169 (3):1239–1260, 2007.

Bensen, G., Ritzwoller, M., and Shapiro, N. M. Broadband ambient noise surface wave tomography across the United States. *Journal of Geophysical Research: Solid Earth*, 113(B5), 2008.

Bertelli, T. *Osservazioni sui piccoli movimenti dei pendoli in relazione ad alcuni fenomeni meteorologici del p.d. Timoteo Bertelli barnabita*. Tip. delle scienze matematiche e fisiche, 1872. https://books.google.fr/books?id=SCZeoq3Z7AQC.

Boué, P. and Tomasetto, L. Opportune detections of global P-wave propagation from microseisms interferometry. *Comptes Ren-

dus. Géoscience, 356(S4):1–16, 2024.

Boué, P., Poli, P., Campillo, M., Pedersen, H., Briand, X., and Roux, P. Teleseismic correlations of ambient seismic noise for deep global imaging of the Earth. *Geophysical Journal International*, 194(2):844–848, Aug. 2013. doi: 10.1093/gji/ggt160.

Brenguier, F., Shapiro, N. M., Campillo, M., Ferrazzini, V., Duputel, Z., Coutant, O., and Nercessian, A. Towards forecasting volcanic eruptions using seismic noise. *Nature Geoscience*, 1(2):126–130, 2008.

Darbyshire, J. and Okeke, E. A study of primary and secondary microseisms recorded in Anglesey. *Geophysical Journal International*, 17(1):63–92, 1969.

Dziewonski, A. M. and Anderson, D. L. Preliminary reference Earth model. *Physics of the earth and planetary interiors*, 25(4): 297–356, 1981.

Ermert, L., Igel, J., Sager, K., Stutzmann, E., Nissen-Meyer, T., and Fichtner, A. Introducing noisi: a Python tool for ambient noise cross-correlation modeling and noise source inversion. *Solid Earth*, 11(4):1597–1615, Aug. 2020. doi: 10.5194/se-11-1597-2020.

Farra, V., Stutzmann, E., Schimmel, M., Gualtieri, L., and Ardhuin, F. Ray-theoretical modeling of secondary microseism P-waves. *Geophysical Journal International*, 206:1730–1739, June 2016. doi: doi: 10.1093/gji/ggw242.

Fukao, Y., Nishida, K., and Kobayashi, N. Seafloor topography, ocean infragravity waves, and background Love and Rayleigh waves. *Journal of Geophysical Research: Solid Earth*, 115(B4), 2010.

GEOSCOPE, French Global Network of broad band seismic stations. Institut de physique du globe de Paris (IPGP) and École et Observatoire des Sciences de la Terre de Strasbourg (EOST), 1982. doi: 10.18715/GEOSCOPE.G.

Gimbert, F. and Tsai, V. C. Predicting short-period, wind-wave-generated seismic noise in coastal regions. *Earth and Planetary Science Letters*, 426:280–292, 2015.

Gualtieri, L., Stutzmann, E., Capdeville, Y., Ardhuin, F., Schimmel, M., Mangeney, A., and Morelli, A. Modelling secondary microseismic noise by normal mode summation. *Geophysical Journal International*, 193(3):1732–1745, June 2013. doi: 10.1093/gji/ggt090.

Gualtieri, L., Stutzmann, E., Farra, V., Capdeville, Y., Schimmel, M., Ardhuin, F., and Morelli, A. Modelling the ocean site effect on seismic noise body waves. *Geophysical Journal International*, 197(2):1096–1106, May 2014. doi: 10.1093/gji/ggu042.

Gualtieri, L., Bachmann, E., Simons, F. J., and Tromp, J. The origin of secondary microseism Love waves. *Proceedings of the National Academy of Sciences*, 117(47):29504–29511, 2020.

Gualtieri, L., Bachmann, E., Simons, F. J., and Tromp, J. Generation of secondary microseism Love waves: effects of bathymetry, 3-D structure and source seasonality. *Geophysical Journal International*, 226(1):192–219, July 2021. doi: 10.1093/gji/ggab095.

Haned, A., Stutzmann, E., Schimmel, M., Kiselev, S., Davaille, A., and Yelles-Chaouche, A. Global tomography using seismic hum. *Geophysical Journal International*, 204(2):1222–1236, 2016.

Hasselmann, K. A statistical analysis of the generation of microseisms. *Reviews of Geophysics*, 1(2):177–210, 1963. doi: 10.1029/RG001i002p00177.

Hersbach, H., Bell, B., Berrisford, P., Hirahara, S., Horányi, A., Muñoz-Sabater, J., Nicolas, J., Peubey, C., Radu, R., Schepers, D., et al. The ERA5 global reanalysis. *Quarterly Journal of the Royal Meteorological Society*, 146(730):1999–2049, 2020.

Igel, J. K. H., Ermert, L. A., and Fichtner, A. Rapid finite-frequency microseismic noise source inversion at regional to global scales. *Geophysical Journal International*, 227(1):169–183, 05 2021. doi: 10.1093/gji/ggab210.

Igel, J. K. H., Bowden, D. C., and Fichtner, A. SANS: Publicly Available Daily Multi-Scale Seismic Ambient Noise Source Maps. *Journal of Geophysical Research: Solid Earth*, 128(1): e2022JB025114, 2023. doi: 10.1029/2022JB025114.

Jiang, C. and Denolle, M. A. NoisePy: A New High-Performance Python Tool for Ambient-Noise Seismology. *Seismological Research Letters*, 91(3):1853–1866, 04 2020. doi: 10.1785/0220190364.

Juretzek, C. and Hadziioannou, C. Where do ocean microseisms come from? A study of Love-to-Rayleigh wave ratios. *Journal of Geophysical Research: Solid Earth*, 121(9):6741–6756, 2016.

Kedar, S., Longuet-Higgins, M., Webb, F., Graham, N., Clayton, R., and Jones, C. The origin of deep ocean microseisms in the North Atlantic Ocean. *Proceedings of the Royal Society A: Mathematical, Physical and Engineering Sciences*, 464(2091):777–793, 2008.

Kennett, B. L., Engdahl, E., and Buland, R. Constraints on seismic velocities in the Earth from traveltimes. *Geophysical Journal International*, 122(1):108–124, 1995.

Kibblewhite, A. C. and Ewans, K. C. Wave–wave interactions, microseisms, and infrasonic ambient noise in the ocean. *The Journal of the Acoustical Society of America*, 78(3):981–994, 1985.

Kozlovskaya, E. Seismic network XK:LAPNET/POLENET seismic temporary array (RESIF-SISMOB), 2007. doi: 10.15778/RESIF.XK2007.

Krischer, L., Megies, T., Barsch, R., Beyreuther, M., Lecocq, T., Caudron, C., and Wassermann, J. ObsPy: a bridge for seismology into the scientific Python ecosystem. *Computational Science and Discovery*, 8(1):014003, may 2015. doi: 10.1088/1749-4699/8/1/014003.

Lecocq, T., Caudron, C., and Brenguier, F. MSNoise, a Python Package for Monitoring Seismic Velocity Changes Using Ambient Seismic Noise. *Seismological Research Letters*, 85(3):715–726, 05 2014. doi: 10.1785/0220130073.

Lecocq, T., Ardhuin, F., Collin, F., and Camelbeeck, T. On the extraction of microseismic ground motion from analog seismograms for the validation of ocean-climate models. *Seismological Research Letters*, 91(3):1518–1530, 2020.

Lin, F.-C., Moschetti, M. P., and Ritzwoller, M. H. Surface wave tomography of the western United States from ambient seismic noise: Rayleigh and Love wave phase velocity maps. *Geophysical Journal International*, 173(1):281–298, 2008.

Longuet-Higgins, M. S. A theory of the origin of microseisms. *Philosophical Transactions of the Royal Society of London. Series A, Mathematical and Physical Sciences*, 243(857):1–35, 1950.

Lu, Y., Stehly, L., Paul, A., and Group, A. W. High-resolution surface wave tomography of the European crust and uppermost mantle from ambient seismic noise. *Geophysical Journal International*, 214(2):1136–1150, 2018.

Meschede, M., Stutzmann, E., and Schimmel, M. Blind source separation of temporally independent microseisms. *Geophysical Journal International*, 216(2):1260–1275, 2019.

Nakata, N., Gualtieri, L., and Fichtner, A. *Seismic ambient noise*. Cambridge University Press, 2019.

Neale, J., Harmon, N., and Srokosz, M. Monitoring remote ocean waves using P-wave microseisms. *Journal of Geophysical Research: Oceans*, 122(1):470–483, 2017.

Nishida, K. Global propagation of body waves revealed by cross-correlation analysis of seismic hum: BODY WAVE PROPAGATION EXTRACTED FROM SEISMIC HUM. *Geophysical Research Letters*, 40(9):1691–1696, May 2013. doi: 10.1002/grl.50269.

Nishida, K. Source spectra of seismic hum. *Geophysical Journal International*, 199(1):416–429, 2014.

Nishida, K. and Takagi, R. Teleseismic *S* wave microseisms. *Science*, 353(6302):919–921, Aug. 2016. doi: 10.1126/science.aaf7573.

Nishida, K. and Takagi, R. A Global Centroid Single Force Catalog of P-Wave Microseisms. *Journal of Geophysical Research: Solid Earth*, 127(4):e2021JB023484, 2022. doi: 10.1029/2021JB023484.

Nissen-Meyer, T., van Driel, M., Stähler, S. C., Hosseini, K., Hempel, S., Auer, L., Colombi, A., and Fournier, A. AxiSEM: broadband 3-D seismic wavefields in axisymmetric media. *Solid Earth*, 5(1): 425–445, 2014.

NOAA National Centers for Environmental Information. ETOPO 2022 15 arc-second global relief model, 2022.

Oliver, J. A worldwide storm of microseisms with periods of about 27 seconds. *Bulletin of the Seismological Society of America*, 52 (3):507–517, 1962.

Poli, P., Campillo, M., Pedersen, H., and Group, L. W. Body-wave imaging of Earth's mantle discontinuities from ambient seismic noise. *Science*, 338(6110):1063–1065, 2012a.

Poli, P., Pedersen, H. A., Campillo;, M., and the POLENET/LAPNET Working Group. Noise directivity and group velocity tomography in a region with small velocity contrasts: the northern Baltic shield. *Geophysical Journal International*, 192(1):413–424, 11 2012b. doi: 10.1093/gji/ggs034.

Retailleau, L. and Gualtieri, L. Toward High-Resolution Period-Dependent Seismic Monitoring of Tropical Cyclones. *Geophysical Research Letters*, 46(3):1329–1337, 2019. doi: 10.1029/2018GL080785.

Retailleau, L. and Gualtieri, L. Multi-phase seismic source imprint of tropical cyclones. *Nature communications*, 12(1):2064, 2021.

Sabra, K. G., Gerstoft, P., Roux, P., Kuperman, W., and Fehler, M. C. Surface wave tomography from microseisms in Southern California. *Geophysical Research Letters*, 32(14), 2005.

Sager, K., Tsai, V. C., Sheng, Y., Brenguier, F., Boué, P., Mordret, A., and Igel, H. Modelling P waves in seismic noise correlations: advancing fault monitoring using train traffic sources. *Geophysical Journal International*, 228(3):1556–1567, 09 2021. doi: 10.1093/gji/ggab389.

Sanchez-Sesma, F. J. and Campillo, M. Retrieval of the Green's Function from Cross Correlation: The Canonical Elastic Problem. *Bulletin of the Seismological Society of America*, 96(3): 1182–1191, 06 2006. doi: 10.1785/0120050181.

Schippkus, S., Safarkhani, M., and Hadziioannou, C. Continuous isolated noise sources induce repeating waves in the coda of ambient noise correlations. *Seismica*, 2023.

Shapiro, N. M., Campillo, M., Stehly, L., and Ritzwoller, M. H. High-resolution surface-wave tomography from ambient seismic noise. *Science*, 307(5715):1615–1618, 2005.

Stehly, L., Campillo, M., and Shapiro, N. M. A study of the seismic noise from its long-range correlation properties. *Journal of Geophysical Research: Solid Earth*, 111(B10), 2006. doi: https://doi.org/10.1029/2005JB004237.

Straume, E. O., Gaina, C., Medvedev, S., Hochmuth, K., Gohl, K., Whittaker, J. M., Abdul Fattah, R., Doornenbal, J. C., and Hopper, J. R. GlobSed: Updated total sediment thickness in the world's oceans. *Geochemistry, Geophysics, Geosystems*, 20(4): 1756–1772, 2019.

Stutzmann, E., Ardhuin, F., Schimmel, M., Mangeney, A., and Patau, G. Modelling long-term seismic noise in various environments. *Geophysical Journal International*, 191(2):707–722, 11 2012. doi: 10.1111/j.1365-246X.2012.05638.x.

The HDF Group. Hierarchical Data Format, version 5. https://github.com/HDFGroup/hdf5.

Tomasetto, L., Boué, P., Stehly, L., Ardhuin, F., and Nataf, H.-C. On the stability of mantle-sensitive P-wave interference during a secondary microseismic event. *Geophysical Research Letters*, 51(8):e2023GL108018, 2024.

UCAR/Unidata. Network Common Data Form (netCDF), 2024, Boulder, CO. doi: http://doi.org/10.5065/D6H70CW6.

Valero Cano, E., Fichtner, A., Peter, D., and Mai, P. M. The impact of ambient noise sources in subsurface models estimated from noise correlation waveforms. *Geophysical Journal International*, 239(1):85–98, 2024.

van Driel, M., Krischer, L., Stahler, S. C., Hosseini, K., and Nissen-Meyer, T. Instaseis: instant global seismograms based on a broadband waveform database. *Solid Earth*, 6(2):701–717, 2015. doi: 10.5194/se-6-701-2015.

Vinnik, L. Sources of microseismic P waves. *Pure and Applied Geophysics*, 103:282–289, 1973.

Wapenaar, K. and Fokkema, J. Green's function representations for seismic interferometry. *GEOPHYSICS*, 71(4):SI33–SI46, 2006. doi: 10.1190/1.2213955.

Weaver, R. and Lobkis, O. On the emergence of the Green's function in the correlations of a diffuse field: pulse-echo using thermal phonons. *Ultrasonics*, 40(1-8):435–439, 2002.

WW3DG. User Manual and System Documentation of WAVEWATCH III version 6.07, The WAVEWATCH III Development Group. *Tech. Note 326 pp. + Appendices, NOAA/NWS/NCEP/MMAB*, 2019.

Xu, Z., Stutzmann, E., Farra, V., and Crawford, W. Theoretical Modelling of Secondary Microseisms Considering Source and Receiver Site Structures, with a Focus on Ocean-Bottom Sediment Effects. *submitted to Journal of Geophysical Research*, 2025.

Zhang, R., Boué, P., Campillo, M., and Ma, J. Quantifying P-wave secondary microseisms events: a comparison of observed and modelled backprojection. *Geophysical Journal International*, 234(2):933–947, 2023.

Ziane, D. and Hadziioannou, C. The contribution of multiple scattering to Love wave generation in the secondary microseism. *Geophysical Journal International*, 217(2):1108–1122, 2019.